Cell

Integrated Structural Analysis of the Human Nuclear Pore Complex Scaffold

Khanh Huy Bui,[1,3] Alexander von Appen,[1,3] Amanda L. DiGuilio,[2] Alessandro Ori,[1] Lenore Sparks,[1] Marie-Therese Mackmull,[1] Thomas Bock,[1] Wim Hagen,[1] Amparo Andrés-Pons,[1] Joseph S. Glavy,[2,*] and Martin Beck[1,*]
[1]European Molecular Biology Laboratory, Structural and Computational Biology Unit, Meyerhofstrasse 1, 69117 Heidelberg, Germany
[2]Department of Chemistry, Chemical Biology and Biomedical Engineering, Stevens Institute of Technology, 507 River Street, Hoboken, NJ 07030, USA
[3]These authors contributed equally to this work
*Correspondence: jglavy@stevens.edu (J.S.G.), martin.beck@embl.de (M.B.)
http://dx.doi.org/10.1016/j.cell.2013.10.055

SUMMARY

The nuclear pore complex (NPC) is a fundamental component of all eukaryotic cells that facilitates nucleocytoplasmic exchange of macromolecules. It is assembled from multiple copies of about 30 nucleoporins. Due to its size and complex composition, determining the structure of the NPC is an enormous challenge, and the overall architecture of the NPC scaffold remains elusive. In this study, we have used an integrated approach based on electron tomography, single-particle electron microscopy, and crosslinking mass spectrometry to determine the structure of a major scaffold motif of the human NPC, the Nup107 subcomplex, in both isolation and integrated into the NPC. We show that 32 copies of the Nup107 subcomplex assemble into two reticulated rings, one each at the cytoplasmic and nuclear face of the NPC. This arrangement may explain how changes of the diameter are realized that would accommodate transport of huge cargoes.

INTRODUCTION

The nuclear pore complex (NPC) regulates the exchange of proteins and RNA between the cytoplasm and nucleoplasm in a highly selective manner. Progress toward elucidating the structure of the NPC has been hampered by its intricate organization and membrane-associated nature. About 1,000 protein molecules are needed to build one of these massive cellular assemblies onto the fused inner (INM) and outer nuclear membranes (ONM). Due to this enormous complexity, the integration of various techniques for structure determination, with the ability to bridge length scales from overall molecular architecture down to atomic resolution, is essential to understand NPC structure (Adams and Wente, 2013). Thus far, X-ray crystallography has provided high-resolution structures of a considerable fraction of the domain folds and some of the protein interfaces (reviewed in Hoelz et al., 2011, for example). Nucleoporins are organized in a modular way and assemble into subcomplexes that, in turn, gather in multiple copies to form 8-fold rotationally symmetric NPCs (Schwartz, 2005). The Nup93 and Nup107 subcomplexes are thought to be essential structural elements of the NPC scaffold. The Nup107 subcomplex has ten members, Nups 160, 133, 107, 96, 85, 43, and 37, Seh1, Sec13, and ELYS, most of which occur isostoichiometrically within NPCs (Ori et al., 2013). Its yeast counterpart consists of seven proteins and was shown to assemble into a Y-shaped structure using single-particle electron microscopy (EM) (Flemming et al., 2010; Kampmann and Blobel, 2009). Despite its central importance to cellular function, the structure of the vertebrate Nup107 subcomplex remains elusive.

The structure of the entire NPC, resolved to ~6.5 nm by cryo-electron tomography (cryo-ET), shows an overall architecture of three rings: the nuclear, spoke, and cytoplasmic rings, all common to higher and lower eukaryotes (Beck et al., 2007; Maimon et al., 2012). A fundamental difference to lower eukaryotes is that during open mitosis in vertebrates, the entire nuclear envelope, including NPCs, is disassembled to allow for chromatin segregation and afterward reassembled (reviewed e.g., in Güttinger et al., 2009). Thereby, Nups are released from the NPC at the onset of mitosis. This event is triggered through phosphorylation by mitotic kinases (Laurell et al., 2011). The majority of all nucleoporin phosphorylation sites specifically occur in mitosis (Olsen et al., 2010). Therefore, dis- and reassembly of the vertebrate NPC might be generally controlled by phosphorylation and dephosphorylation, respectively. The human Nup107 (hNup107) subcomplex is released as a whole and stabilized for subsequent NPC reassembly, whereas several of its members are phosphorylated (Glavy et al., 2007). One might thus assume that its intersubcomplex protein interfaces, which are relevant for higher order scaffold assembly, are a specific target for phosphorylation, although this hypothesis has never been practically tested.

Determination of subcomplex organization relative to overall NPC architecture in a higher eukaryote is thus critical in the progression toward an understanding of NPC assembly mechanisms. Thus far, several conceptual models of the yeast NPC

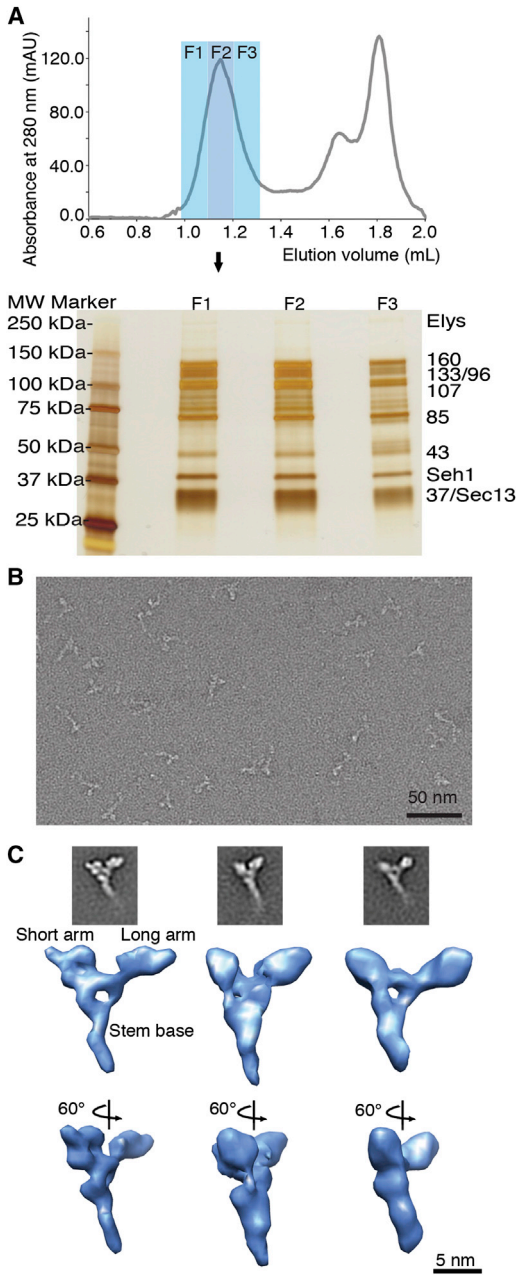

Figure 1. Isolation and Structural Analysis of the Human Nup107 Subcomplex

(A) Gel filtration of affinity-purified hNup107 subcomplex resulted in a single elution peak that contained all ten members as determined by shotgun proteomics (data not shown) and SDS-PAGE.

(B) Negative staining electron micrograph of the eluted species after gel filtration. Single particles display the typical Y-shape.

(C) Representative class averages of the Nup107 subcomplex obtained by subtomogram averaging focused to the vertex element. The vertex has a long and short arm and a characteristic lower density in the center region. The stem was averaged out.

See also Table S1, Figure S1, and Movie S1.

were put forward. (1) Based on similarity to vesicle coat proteins, the lattice model proposed that the long axis of the yNup84 subcomplex follows the curvature of the fused INM and ONM (Brohawn et al., 2008). (2) Based on crystal structures of yNup85-Seh1 and ySec13-Nup145C, the fence-pole model proposed that 32 copies of the yNup84 subcomplex form four antiparallel rings stacked onto each other (Debler et al., 2008). (3) By combining various experimental data into a computational model, it was suggested that 16 yNup84 subcomplexes are arranged head to tail into two rings at the cytoplasmic and nuclear face of the NPC (Alber et al., 2007). Biochemical and advanced imaging studies support a head-to-tail arrangement of the yNup84 (Kampmann et al., 2011; Seo et al., 2009) and hNup107 subcomplexes (Kampmann et al., 2011; Szymborska et al., 2013). Therefore, whereas previous work provides substantial insight into this complex puzzle, the lack of direct structural evidence for the arrangement of the Nup107 subcomplex and its yeast counterpart leads to lingering debate over their exact 3D orientation and stoichiometry.

Particular obstacles to experimentally determine the position of subcomplexes within the NPC were that (1) the resolution of tomographic maps of the entire NPC was insufficient to fit in single-particle structures obtained from isolated subcomplexes, and (2) classical interaction screening methods failed to discriminate between intra- and intersubcomplex protein contact sites. In this study, we overcome these obstacles by integrating several techniques that bridge the various length scales. Our structural reconstruction elucidates how 32 copies of the hNup107 subcomplex form the NPC scaffold within the nuclear and cytoplasmic rings of the NPC in a previously unanticipated manner. We show that phosphorylation predominantly occurs in the intersubcomplex interfaces and thus is very likely to directly control stepwise NPC assembly. Thus, we provide a blueprint for the molecular organization of one of the NPCs essential scaffold components within the entire architecture.

RESULTS

Structure of the Human Nup107 Subcomplex

To structurally analyze the hNup107 subcomplex, we affinity-purified it from human tissue culture cells that were nocodazole-arrested to release it from the NPC. All ten members of the hNup107 subcomplex copurified with ELYS being apparently less stably associated (Figure 1A). To validate whether the purified hNup107 subcomplex was natively phosphorylated, we performed a phosphoproteomic analysis. We identified 78 phosphorylation sites, 48 of which were previously unknown (Table S1 available online). Most phosphorylation sites were identified in ELYS, Nup133, and Nup96 (19, 18, and 17 sites, respectively).

We next obtained a 3D structure of the isolated hNup107 subcomplex. We first acquired electron tomograms of single particles embedded in thick negative stain to allow for their intact and nonflattened structure. Although the human Nup107 subcomplex is overall Y shaped as its yeast counterpart (Kampmann and Blobel, 2009), it appeared much more flexible on the single-molecule level (Figure S1). To cope with this flexibility, during structural analysis, the reconstruction was focused to the static

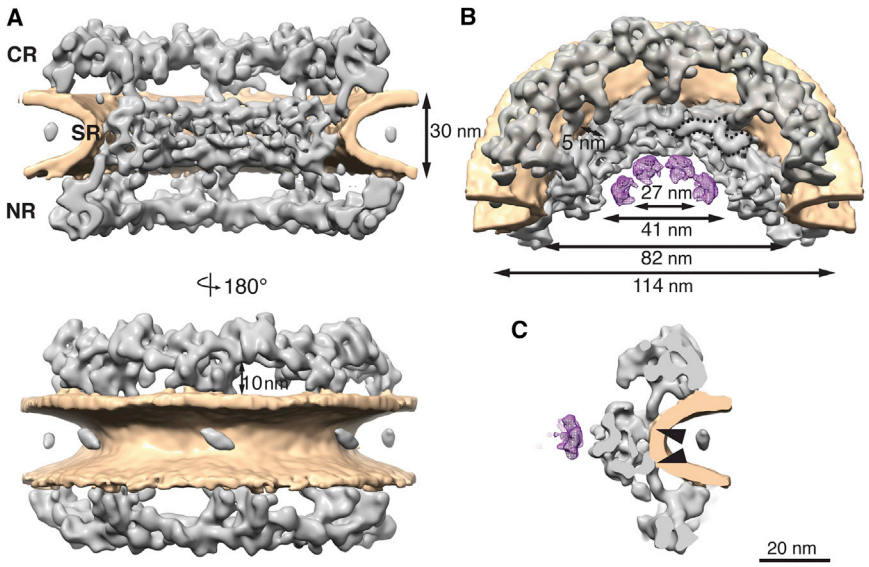

Figure 2. Cryo-EM Structure of the Human NPC at 3.2 nm Resolution

(A) Isosurface-rendered view of the human NPC (cut in half) in two different orientations. Membranes are rendered yellow; the cytoplasmic (CR), spoke (SR), and nuclear rings (NR) are marked.

(B) Same as (A) but seen as top view. An additional inner ring density (purple) is apparent only at lower isosurface threshold. This density is more delineate than the spoke ring indicating high structural plasticity. Crescent shapes similar to the structures of some members of the Nup93 subcomplex are highlighted with dots in (B); openings that might be relevant for the INM protein import are indicated in (A) and (B).

(C) The spoke ring complex connects to the membrane at two distinct sites per asymmetric unit (arrowheads), which are continuous with a C2-symmetric connection to the cytoplasmic and nuclear rings.

See also Figure S2.

region—namely, both arms and the stem base, hereafter referred to as vertex in agreement with the yeast terminology (Kampmann and Blobel, 2009). The vertex was nicely resolved in our 3D map, whereas the flexible stem was averaged out (Figures 1C and S1). The long and short arms are not in a strictly planar arrangement in all classes but can bend slightly out of the vertex plane (Figure 1C; Movie S1). To quantify the flexibility of the stem, we manually analyzed about 100 subtomograms containing individual single particles (Figures S1C–S1E). We found that the hNup107 subcomplex contains four distinct hinges that can bend up to angles of 90° and assume a multitude of different conformations. Fully stretched, it could bridge a distance of up to 56 nm measured from the longer arm of the vertex to the tip of the stem. As compared to the previously analyzed yNup84 subcomplex (Kampmann and Blobel, 2009), the stem of the hNup107 subcomplex is longer, both the stem and vertex appear more flexible, additional density is observed in both arms, and the branching element has a region of lower density in its very center (Figures 1 and S1).

Tomographic Structure of the Human NPC Resolved to 3.2 nm

A considerable impediment to elucidating the NPC scaffold arrangement was that structures of isolated subcomplexes and fully assembled NPCs were previously not available at sufficient resolution for direct comparison. We therefore used cryo-ET to generate a better-resolved structural framework of the human nuclear pore. We based our study on nuclear envelopes (NEs) purified from human HeLa cells, which contain fully intact, transport competent NPCs (Ori et al., 2013). We have previously determined the copy number of all Nups per NPC in HeLa cells (Ori et al., 2013). The investigated NPC species are therefore compositionally defined. We acquired 269 tomograms, each containing about five NPCs on average, which corresponds to more than 10,000 asymmetric units. The structure of the NPC asymmetric unit was determined as described previously (Beck et al., 2007) with minor modifications. Based on this analysis, we could enhance the resolution of the scaffold structure up to 32 Å (3.2 nm, Figures 2 and S2).

Our structure shows that the nuclear and cytoplasmic rings have an inner diameter of 84 nm. They are connected to the spoke ring through two C2-symmetric rod-shaped connectors per asymmetric unit (Figures 2B and 2C), in agreement with previous work (Maimon et al., 2012). The connectors themselves form touching points with the membrane (Figure 2C), whereas another two touching points per asymmetric unit are found in both the cytoplasmic and nuclear rings (see below). The spoke ring complex has an inner diameter of 41 nm that defines the constriction of central channel. Within the central channel, less delineate electron optical density with an inner diameter of 27 nm is apparent at lower isosurface threshold levels, which most probably accounts for flexible elements (Figures 2B and 2C). These observations are consistent with the previously reported size limit of cargo (Panté and Kann, 2002) and the suggested dynamic nature of the central transporting module (Beck et al., 2004; Schwarz-Herion et al., 2007; Solmaz et al., 2011).

Four Vertices per Asymmetric Unit Are Positioned in the Nuclear and Cytoplasmic Rings

To localize the hNup107 subcomplex within the scaffold, we performed a systematic, template-matching-based search for the position and orientation of the highly ordered vertex within the tomographic electron optical density of one subunit of the NPC. We repeated the fitting procedure with 30,000 random starting positions and consistently identified two pairs of exactly C2-symetric positions in the nuclear and cytoplasmic rings with very high cross-correlation values as the top four hits (Figures 3A, 3B, and S3). We note that those top four hits comprise independent identifications because C2 symmetry was not imposed during the subtomogram alignment process. All other hits had considerably lower cross-correlation values, caused clashes, and were not C2 symmetric (Extended Experimental Procedures). To objectively assess the structural similarity of the

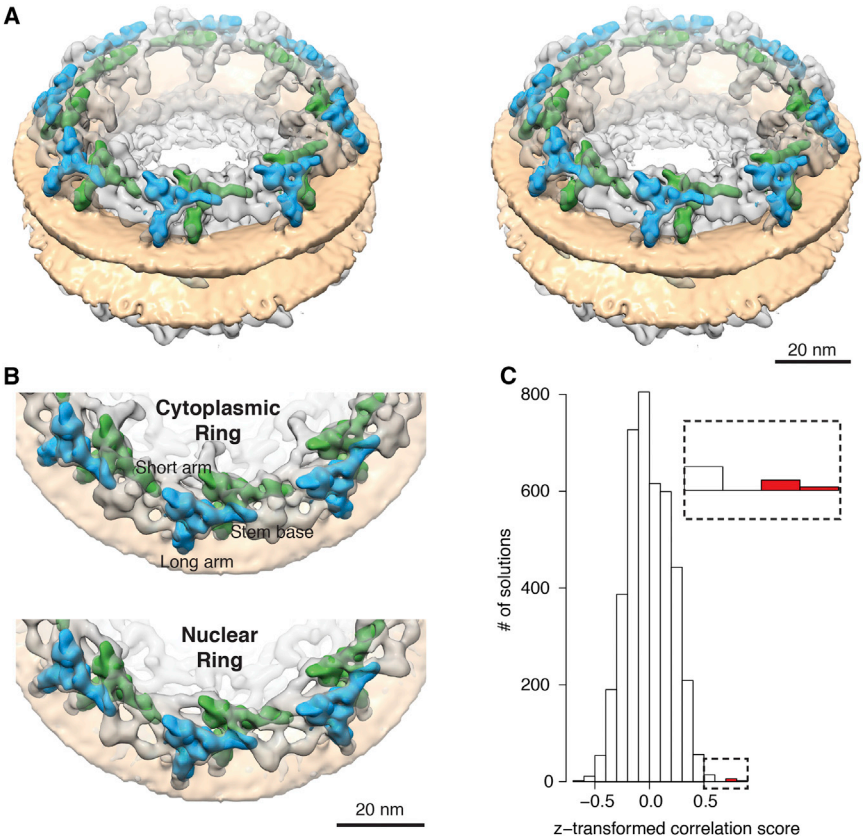

Figure 3. Positioning of the Vertex of the hNup107 Subcomplex within the NPC Scaffold

(A) Stereoview of the optimized fit of the two vertices per subunit in the cytoplasmic ring (protein in transparent gray, membranes in yellow, the two fitted vertices per subunit in green and blue).

(B) The same as top view for the cytoplasmic (top) and the nuclear rings (bottom).

(C) Histogram of the z-transformed correlation score of all obtained fits. The top four hits (red, highlighted in the inset) occur C2 symmetrically within the cytoplasmic and nuclear rings (see also Figure S3B) and are clearly discriminated from the (false-positive) score distribution.

See also Figure S3.

isolated vertex to all the matched positions, we employed a statistical analysis that derives the likelihood for each of the matched positions to be a false positive. The score distribution of all matched positions shows that the four top hits are clearly discriminated from the false-positive distribution (Figure 3C). All four identified positions are thus true-positive hits (p values: 0.00026, 0.00073, 0.00118, and 0.00125, respectively).

Strikingly, the electron optical density observed within the tomographic map is almost indistinguishable from the vertex structure of the isolated hNup107 subcomplex. Even detailed features of the structural signature of the isolated vertex are clearly resolved in all instances of the tomographic map, including the shape of both arms, the small extension at the tip of the short arm, the angles of arms and stem, as well as the lower density region of the branching element (Figures S3A and S4B, Movie S2). This finding is very much in line with the previously determined stoichiometry that detected 32 copies of the hNup107 subcomplex per NPC (Ori et al., 2013), corresponding to 16 copies within each cytoplasmic and nuclear ring. Both vertices are oriented at an angle of 55° to the nuclear envelope plane with the longer arm facing the membrane. The two vertices are shifted toward each other by about 11 nm, such that the branching element of the inner vertex is positioned behind the stem base of the outer vertex (Figures 3A and S3). The conformation of the corresponding stems is not immediately obvious from the observed electron optical density.

Similarity of the Cytoplasmic and Nuclear Rings

To determine the conformation of the stems, we calculated a consensus map of the aligned tomographic structures of the cytoplasmic and nuclear rings (Figure 4; Movie S2). In contrast to commonly used difference maps, only consistent features are retained in the consensus map, whereas variable features are diminished. Scaffold Nups, including the members of the hNup107 subcomplex, are C2 symmetrically distributed (Krull et al., 2004; Rout et al., 2000) and will thus consistently contribute to the electron optical density observed in both rings. In contrast, transport channel Nups are often asymmetrically distributed across the nuclear envelope plane. In particular, Nup358, Nup214, Nup88, Aladin, and hCG1 localize to the cytoplasmic ring, whereas Nup153, Nup50, and TPR localize to the nuclear ring (reviewed in Schwartz, 2005, for example). Therefore, structured domains of asymmetric transport channel Nups will contribute unevenly to the electron optical density of the nuclear and cytoplasmic rings, whereas their flexible domains are generally averaged out. They are thus underrepresented in the consensus map, whereas the electron optical density of static scaffold features will be enhanced. Indeed, this analysis distilled out two Y-shaped densities per subunit per ring that closely resemble the orientations of the fitted subcomplex, including both stems. This finding independently confirms positioning of the vertices. The consensus map suggests that both stems horizontally reach to the adjacent subunit in a bent conformation that is in agreement with the hinge positions detected in our single-particle analysis of the isolated hNup107 subcomplex (Figures 4B and 4C; Movie S2). This arrangement elegantly unifies previous experimental evidence from various sources, including Nup stoichiometries (Ori et al., 2013), molecular weight measurements (Reichelt et al., 1990), as well as imaging (Kampmann et al., 2011; Krull et al., 2004; Ori et al., 2013; Paulillo et al., 2005; Szymborska et al., 2013) and biochemical data (Seo et al., 2009).

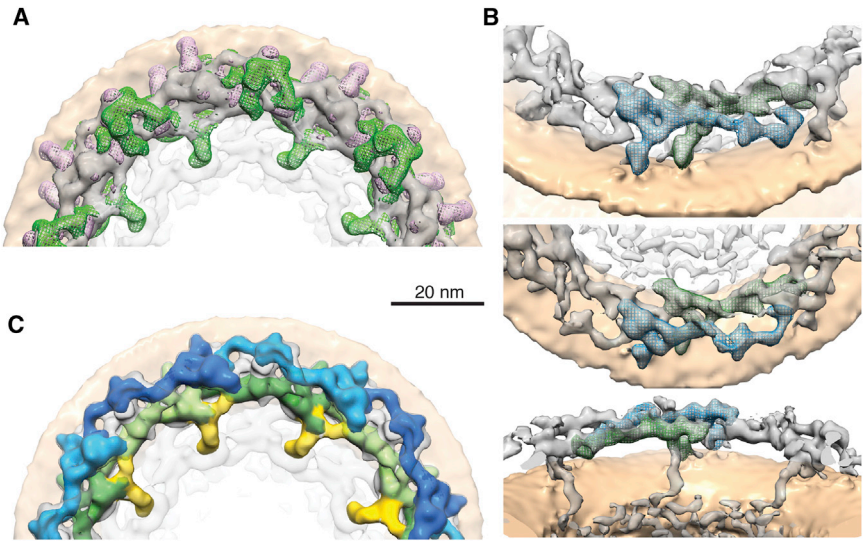

Figure 4. Consensus Map of the Cytoplasmic and Nuclear Rings and Localization of the Nup214 Subcomplex

(A) Top view of the consensus map. Electron optical density that is consistent between the cytoplasmic and nuclear rings is shown gray; densities specific to the cytoplasmic or nuclear rings are shown as green or purple meshes, respectively.

(B) The three panels show the consensus map superimposed with the segmented position of the hNup107 subcomplex at three different orientations. Essentially only two instances of the hNup107 subcomplex are represented in the map. For clarity, the threshold for the isosurface rendering has been slightly reduced (see also Movie S2).

(C) The Nup214 subcomplex was localized by difference mapping of NPCs with a reduced abundance of the Nup214 subcomplex to the wild-type and occupies a protrusion specific to the cytoplasmic ring. Differential density is shown in yellow; the hNup107 subcomplexes are segmented in green and blue (see also Figures S4C and S4D). See also Figure S4 and Movie S2.

Localization of the Nup214 Subcomplex

Our structural model explains 62% of the electron optical density of the cytoplasmic ring and 91% of the consensus map. The remaining density is expected to arise primarily from the structured domains of asymmetric Nups. To investigate if the proposed scaffold structure remains unaffected when transport channel Nups are removed, we generated a stable cell line that inducibly expresses a micro-RNA engineered to silence *nup214*. When induced, the abundance not only of Nup214 but also of Nup88, which is in the same subcomplex, was reduced by more than 50% (Figure S4). The other two members of the same subcomplex, Nup98 and Nup62, also show reduced abundance, although less pronounced because most copies of these two Nups are part of other, unaffected subcomplexes. We thus conclude that the stable cell line forms NPCs with a reduced abundance of the Nup214 subcomplex.

A tomographic structure obtained from such NPCs showed reduced electron optical density in a protrusion of the cytoplasmic ring outside of the scaffold structure (Figures 4C and S4C). This result is supported by the consensus map analysis, in which the same protrusion is identified as exclusive cytoplasmic density (Figure 4A). This analysis emphasizes that the short axis of the hNup107 subcomplex cannot be orientated in parallel to the NE plane, as previously assumed, but is tilted by 55°.

Crosslinking MS Confirms the Structural Organization of the NPC Scaffold

Finally, we validated our structural model by obtaining distance constraints of inter- and intrasubcomplex interactions using crosslinking mass spectrometry (XL-MS). We used isotope-coded disuccinimidyl-suberate for specific lysine crosslinking and subsequent identification using the xQuest/xProphet tool as previously described (Walzthoeni et al., 2012). We applied XL-MS to both isolated subcomplexes and intact NPCs to systematically identify nucleoporin interfaces. Crosslinks that are identified in isolated subcomplexes must be intrasubcomplex contacts. Crosslinks that are identified from intact NPCs can potentially be both intra- and intersubcomplex contacts.

We first analyzed the purified hNup107 subcomplex by XL-MS and identified 32 nonredundant interprotein crosslinked peptides within the subcomplex (Figure 5A, Table S2, and Data S1). These spatial restraints taken together with the shape of the available X-ray structures and homology models (Table S3) allowed us to confidently annotate most of the electron optical density of the vertex with high-resolution structures, whereas the respective structures of the stem (Nup107 and Nup133) can only be approximately positioned (Figure 5B; Extended Experimental Procedures). The majority of all spatial restraints are satisfied by our model (Table S2). The localization of the seven conserved Nups within the subcomplex is consistent with the lower eukaryotes (Nagy et al., 2009; Thierbach et al., 2013). The actual branching element of the vertex is not annotated because the respective domain folds were not yet analyzed by X-ray crystallography (Figure 5B). Our XL-MS analysis reveals that Nup96 forms this branching element through interactions with Nup85 and Nup160 to the respective arms of the vertex as well as multiple contacts to ELYS (Figures 5B and S5).

To identify intersubcomplex restraints, we next obtained XL-MS data of intact NPCs. To this end, we again used NEs purified from HeLa cells, a sample of moderate proteomic complexity that is highly enriched for intact nuclear pores. The identification of crosslinked peptides from such samples imposes a considerable challenge because of the potential number of possible peptide combinations. We therefore reduced the sample complexity by extensive 3D peptide fractionation using isoelectric focusing, gel filtration, and online reversed phase chromatography. As an alternative, complementary approach, we crosslinked purified, intact nuclei and subsequently affinity-purified the crosslinked Nups under denaturing conditions. The combined data set contained 17 interprotein crosslinked peptides (Table S2; Figure 5). Several of the identified contacts account for already described inter- and intrasubcomplex interactions, including crosslinks formed by Nup62-Nup93 (Sachdev et al., 2012),

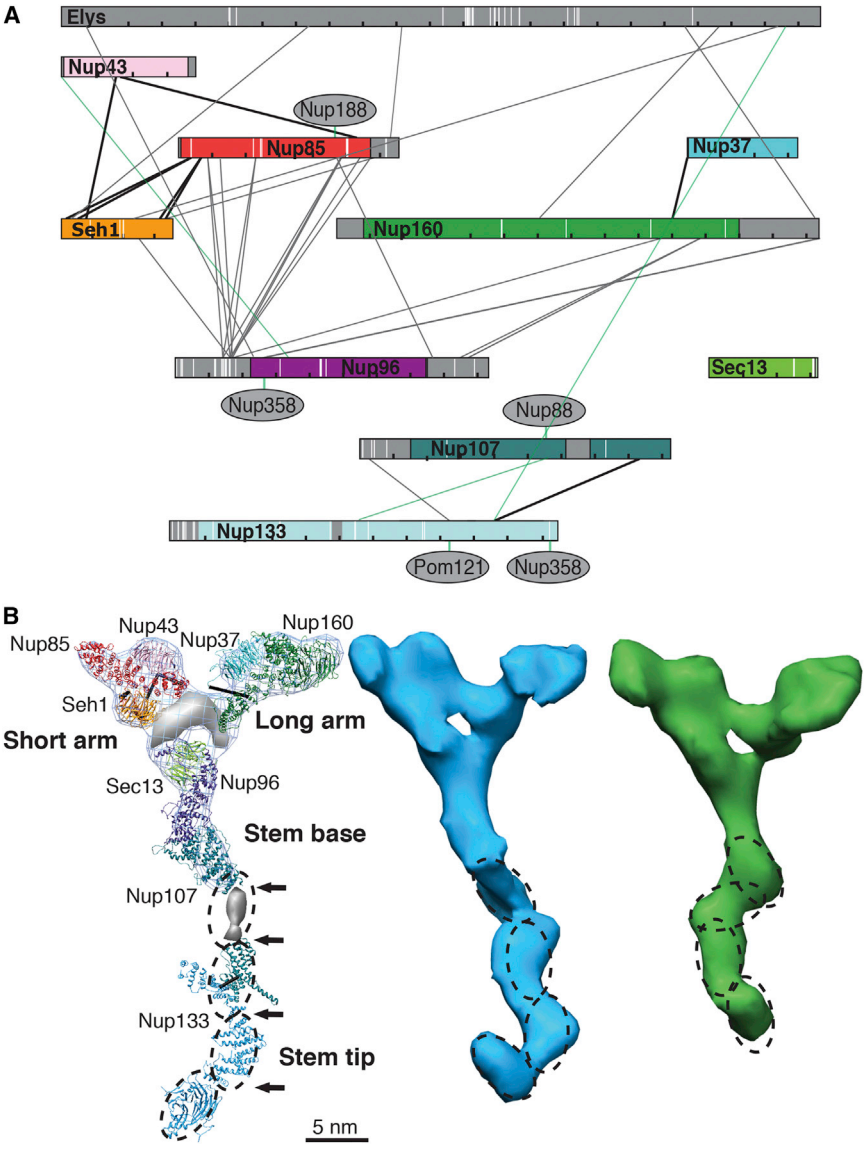

Figure 5. Structural Analysis of hNup107 Subcomplex and Nuclear Pores by Crosslinking Mass Spectrometry

(A) The spatial restraints identified by XL-MS are shown as connections between the primary structures of the Nup107 subcomplex proteins. Spatial restraints that map into available crystal structures are shown in black. Crosslinks accounting for verified intersubcomplex interactions within the hNup107 subcomplex as well as intersubcomplex interactions with other NPC components are shown in green; crosslinks not covered by the structural models are shown in gray. The positions of the phosphorylation sites identified within the hNup107 subcomplex are represented as white lines within the primary structures.

(B) The structural model of the isolated hNup107 subcomplex is shown side by side with the inner and outer Nup107 subcomplex segmented from the tomographic map. The available crystal structures and homology models were fitted into or localized with respect to the electron microscopy structure of the vertex based on their shape and spatial restraints obtained by crosslinking mass spectrometry (XL-MS) that are shown as black lines. Some protein interfaces were previously analyzed by X-ray crystallography and are thus represented at high resolution, whereas others were modeled at lower resolution according to spatial restraints. The rotation of the X-ray structures of the stem around the stem axis cannot be determined (color-code matches, A; Extended Experimental Procedures). The four arrows and dashed ellipses indicate the position of the flexible hinges and static connectors, respectively (Figure S1). ELYS binds to both arms of the vertex (as shown in A) but is not represented in (B) because its density was averaged out during the structural analysis (because of its underrepresentation). Two regions for which no crystal structures are available are shown isosurface rendered, the branching region bright gray (Nup96) and the middle of the stem in dark gray (Nup107).

See also Figure S5 and Tables S1, S2, and S3.

Nup155-POM121 (Mitchell et al., 2010) as well as Nup53-Nup93, Nup205-Nup93, and Nup155-Nup93 (Mansfeld et al., 2006; Miller et al., 2000), respectively. We also identified several crosslinks likely accounting for intra-Nup107 subcomplex contacts, including restraints in Nup43-Seh1, ELYS-Nup160, and ELYS-Seh1, which are in part redundant with the above-described analysis. Interestingly, we also found crosslinks of Nup133-Nup107, Nup96-Nup43, and ELYS-Nup133. The respective protein contact sites are far apart within one subcomplex but close together in adjacent subcomplexes within the NPC scaffold (Figure 6). We confirmed the absence of these restraints in isolated subcomplexes based on quantification of extracted precursor ion chromatograms. They thus account for intersubcomplex contacts that further confirm our NPC scaffold structure derived from electron microscopy. Additional spatial restraints identified by XL-MS and independent previous evidence facilitated the assignment of electron optical density observed outside of the hNup107 subcomplex and allowed us to localize the potential binding regions of POM121, Nup188, and Nup358 (Figures 6B–6D; Extended Experimental Procedures). In these cases, we cannot exclude the possibility that other proteins bind to the same region of the NPC. Interestingly, we identified a spatial restraint formed in Nup88-Nup107, which confirms the region identified from our knockdown cell lines as the Nup214 subcomplex-binding site.

Based on the XL-MS data, the electron optical density of the tomographic map, the size and shape of the available X-ray structures, and the above-described flexible hinge positions, we conclude that the two stems are most likely arranged in the following way. The stem that emanates from the inner vertex has a spring-shaped conformation and forms a head-to-tail interaction with the interface of the inner and outer vertices of the adjacent subunit. The stem emanating from the outer vertex exhibits a slightly bent conformation that protrudes toward

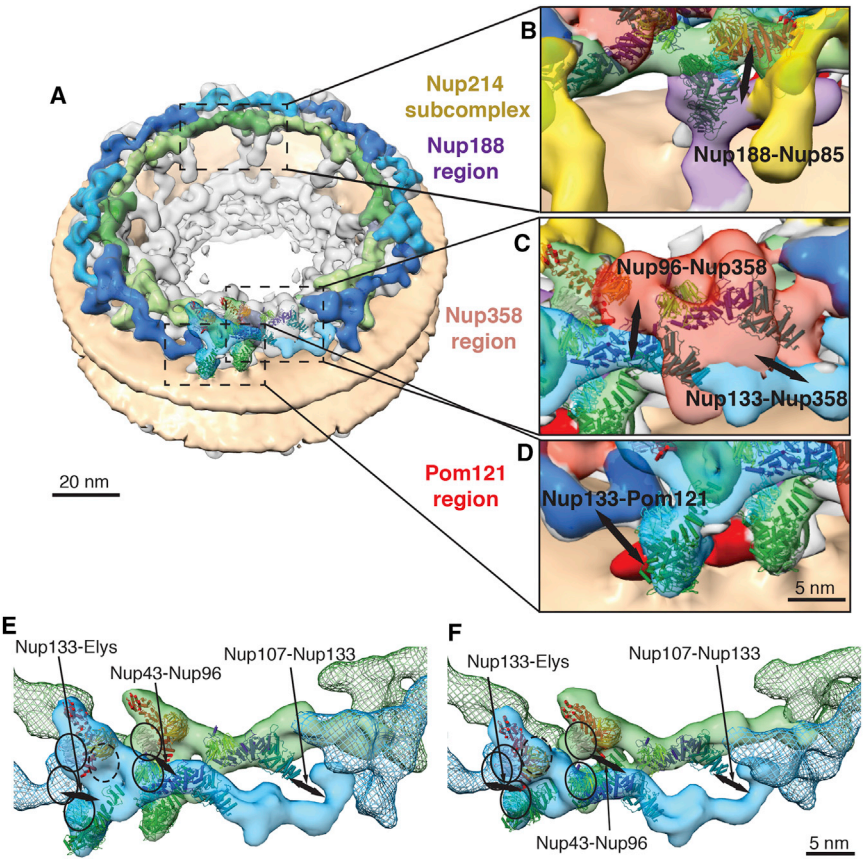

Figure 6. Structural Model of the Cytoplasmic Ring of the Human NPC

(A) Visualization of the orientation of the hNup107 subcomplex within the cytoplasmic ring. The tomographic map is shown isosurface rendered. The segmented outer and inner vertices are shown superimposed in blue and green, respectively. The X-ray structures of the vertex were positioned into the tomographic map according to the fit of the isolated vertex (Figure 3) and their position within the isolated vertex (Figure 5).

(B–D) Zoomed-in views highlighting specific regions of the cytoplasmic ring (framed in A). Spatial restraints identified by XL-MS are shown as black, double-headed arrows. (B) The positioning of Nup188 region (violet) and the Nup214 subcomplex (yellow) are shown for two adjacent subunits. Nup188 is likely part of the density connecting the cytoplasmic and spoke rings (evidence based on spatial restraints placing Nup188 into the proximity of Nup85 and Nup62 [Table S2], NPC stoichiometry [Ori et al., 2013] and consensus map). (C) Additional density is observed on top of the Nup96 region (highlighted in dark orange) that is likely occupied by the N-terminal, structured domain of Nup358 (evidence based on two spatial restraints [Table S2] and consensus map). (D) Additional density in the Nup160 region (highlighted in red) is likely occupied by the N-terminal domain of POM121 that stretches from Nup160 to Nup133 (evidence based on one spatial restraint [Table S2] and one known interaction of POM121; Mitchell et al., 2010).

(E and F) The position of the intersubcomplex crosslinks of the hNup107 subcomplex is shown superimposed the segmented density of the consensus map. The restraints map either into regions not yet structurally analyzed or the flexible hinges, but they are plausible only across multiple structural instances of the hNup107 subcomplex, but not within one subcomplex (ELYS-Nup133 likely relevant only for the nuclear ring). Beta-propellers proximities that most likely account for the critical intersubcomplex contacts are highlighted. Nup133 of inner subcomplex (dashed line) is in close proximity with Nup133 of the outer subcomplex as well as Nup43 and Nup37 to form head-to-tail contacts, whereas Nup43 and Sec13 form a nexus between both vertices.

See also Figure S6 and Movie S3.

Nup160 of the next outer vertex (Figures 5B, 6E, and 6F; Movies S2 and S3). Although the position of the X-ray structures contained in the vertices can be localized within the tomographic map based on the fit of the single-particle structure (Figure 6A), this is not as straightforward for the stem tip because it is not clear which conformation of the hinges the available X-ray structures correspond to. Thus, we visualized the approximate positions of Nup133 and Nup107 in the tomographic map but did not fit in the respective X-ray structures.

DISCUSSION

Our data strongly suggest that 32 copies of the Nup107 subcomplex form a reticulated ring scaffold at both, the cytoplasmic and nuclear face of the NPC that is decorated with functional transport channel Nups (Figure 7). One might thus speculate that this arrangement evolutionarily arose through duplication of a single-ringed ancestor. The structural model aids a better understanding of various NPC-associated processes.

Implications for NPC Assembly

The position of POM121 explains its early recruitment during interphase assembly (Dultz and Ellenberg, 2010) in order to fuse the INM and ONM (Talamas and Hetzer, 2011). The subsequent recruitment of the Nup107 subcomplex through interaction of POM121 with Nup160 might be the first step to associate the vertex interface. The intersubcomplex interface is then probably strengthened by interactions between Nup43 and Nup96/Sec13 as well as Nup96 and Nup133, respectively, as suggested by direct touching points observed in the tomographic map (Movie S3), although this remains to be ultimately clarified by high-resolution structural analysis in the future. These events are likely controlled by phosphorylation because the majority of all nucleoporin phosphorylation sites specifically occur in mitosis (Olsen et al., 2010), and the initial steps of nuclear envelope breakdown are controlled by kinases (Laurell et al., 2011). Interestingly, we detected multiple phosphorylation sites in the relevant contact region of Nup160 that might be functionally relevant for NPC assembly (Figure S5A). Also, the very N terminus of Nup133 is heavily phosphorylated, likely to control the

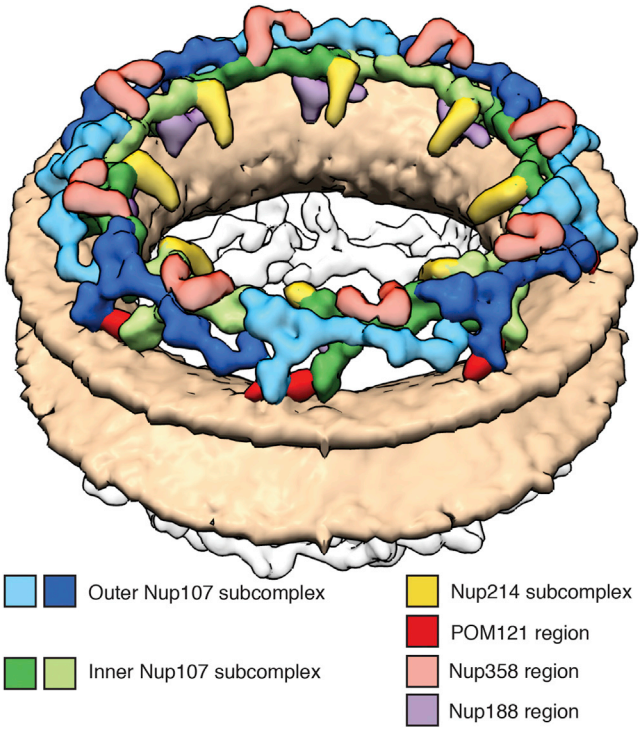

Figure 7. Illustration Visualizing the Three-Dimensional Arrangement of the hNup107 and Its Adjacent Subcomplexes within the NPC Scaffold

All 16 copies of hNup107 subcomplex within the cytoplasmic ring are shown. The inner and outer instances are colored green and blue, respectively. Adjacent Nups and subcomplexes are shown color coded.

head-to-tail interaction of the hNup107 subcomplex. The N-terminal part of Nup96, which appears highly flexible in isolated subcomplexes, is heavily phosphorylated suggesting that it might assume a different conformation in assembled NPCs, where it localizes into the vertex interface. Overall, the majority of all phosphorylation sites detected within the hNup107 subcomplex (>90%) map to the branching element, the two arms, and the tip of the stem, suggesting that the association of inter-subcomplex interfaces is directly phosphorylation controlled.

Nucleoporin ELYS has been previously suggested to localize asymmetrically to the nuclear ring because of its chromatin binding properties (Rasala et al., 2006) and substoichiometric occurrence in the nuclear pore (Ori et al., 2013). Because it did not stably copurify with our hNup107 subcomplex isolations, it will not contribute density to the structure of the isolated vertex. Strikingly, our consensus map analysis shows additional density in the Nup160 region that exclusively occurs in the nuclear ring (Figure S4A). This density very likely accounts for the structured N-terminal domains of ELYS, which is consistent with previous structural analysis (Bilokapic and Schwartz, 2012) and our cross-linking data. ELYS is thus ideally positioned at the very periphery of the scaffold to reach out for chromatin interactions.

The position of Seh1 in the short arm does not imply a direct role in the NPC scaffold and is consistent with other observations: Seh1 might be less stably associated with the Nup107 subcomplex in higher eukaryotes (Loïodice et al., 2004; Ori et al., 2013) and is even dispensable under certain circumstances (Senger et al., 2011). Gene silencing implied a role for Nup107 subcomplex associated Seh1 in open mitosis (Loïodice et al., 2004). Interestingly, Nup43, which is absent in yeast, assumes a position opposite to Seh1 at the short arm that seems essential for human NPC scaffold formation. One might thus speculate whether Nup43 assumes a previous role of Seh1, whereas in vertebrate systems Seh1 has evolved to fulfill a different function during open mitosis.

Conservation of NPC Architecture

Despite sharing the overall Y-shape, the hNup107 subcomplex shows remarkable differences to the yNup84 subcomplex. The stem of the hNup107 subcomplex is considerably longer and much more flexible. It can assume a multitude of different conformations, whereas the yNup84 subcomplex was shown to exist in two predominant stem conformations (Kampmann and Blobel, 2009). Interestingly, the angular arrangement of the short and long arms is drastically different between the two species (72° versus 96°; Figure S4B). These structural differences are such that the yNup84 subcomplex structure cannot be fitted into the tomographic map of the human NPC without causing massive clashes. To deduct conclusions for the lower eukaryotic architecture from the presently available electron microscopic information would thus be speculative.

It has been previously shown that the cytoplasmic and nuclear ring structures can be isolated from intact vertebrate NPCs (Akey, 1989; Unwin and Milligan, 1982). Indeed, the head-to-tail contacts seem sufficient to stabilize an isolated ring because the connections to the spoke ring complex bind only to the periphery of the hNup107 subcomplex but do not interrupt the ring arrangement. In contrast to the lower eukaryotic *Dictyostelium* NPC, in which one rod-shaped element per asymmetric unit directly connects the cytoplasmic and nuclear rings through both membranes (Beck et al., 2007), the luminal density of the human NPC is less delineate but in striking agreement with previous reconstructions (Akey, 1989; Akey and Radermacher, 1993) and super-resolution experiments that localized gp210 (Löschberger et al., 2012).

Structural Plasticity

Strikingly, the double-ring arrangement of the hNup107 subcomplex offers an explanation for structural plasticity of the NPC that was previously observed, including variable diameters (Akey, 1995; Beck et al., 2007; Goldberg and Allen, 1993) and even different rotational symmetries (Hinshaw and Milligan, 2003). The arrangement in which the two vertices per subunit are connected by flexible and spring-shaped hinges provides a rationale for how such changes are potentially realized and might provide robustness to mechanical stress. Such large-scale rearrangements might be biologically relevant, e.g., for the transport of huge cargoes.

Relationship to Vesicle Coats

A potential evolutionary relationship and architectural similarity of the NPC scaffold to vesicle coats has been previously discussed (Brohawn et al., 2008; Devos et al., 2004). Our structural

model reveals that hNup107 subcomplexes form two shifted head-to-tail rings on a flat membrane surface, which is remarkably different from the architectural organization of COPI, COPII, and clathrin proteins. Nevertheless there are parallels. Similarly to COPII-coated vesicles, the scaffold is assembled through interaction hubs formed by β-propeller folds, namely, of Nup133 with Nup37 and Nup43 (head to tail), as well as Nup43 and Sec13 (vertex interface; Figures 6E and 6F). In the case of COPII, the actual scaffolding cage is held at a certain distance from the membrane by specific adaptor proteins that have membrane touching points. Because these adaptor proteins are attached to the coat but not directly integrated into it, coat elements can preassemble without them (Stagg et al., 2006). In the case of the NPC, Nup160 seems to work as a membrane-connecting spacer. However, Nup160 is directly engaged into essential scaffold contacts and thus is not an adaptor protein.

As the Nup107 subcomplex occupies a large portion of the cytoplasmic and nuclear rings, the Nup93 subcomplex is likely to compose the majority of the spoke ring, as previously implied by gold-labeling studies (Krull et al., 2004). Interestingly, the lipid bilayer is continuously resolved at the membrane touching points of the spoke ring complex in our tomographic structure, whereas the outer lipid layer is not apparent below Nup160 (Figure S6). This finding underlines that the Nup107 and Nup93 subcomplexes might have very different membrane binding modes.

In our tomographic map structural features that might resemble the distinctive crescent shapes of certain members of the Nup93 subcomplex (Amlacher et al., 2011) are observed in the spoke ring (Figure 2B). However, because these proteins have very similar folds but do not occur isostoichiometrically within the NPC (Ori et al., 2013) it would be speculative to assign this density to specific proteins. The observed crescent shapes hold up openings within the spoke ring that were previously discussed to be relevant for the import of INM proteins (Antonin et al., 2011) and would allow passage of globular domains up to a size of 5 nm. They thus define the smallest constriction because the elevation of the cytoplasmic and nuclear rings from the ONM and INM, respectively, leaves openings of about 10 nm (Figure 2).

Implications for the Transport Mechanism

The flexible phenylalanine-glycine (FG) repeat containing domains of several different transport channel Nups facilitate the exchange of cargo complexes in a not-yet fully understood transport mechanism. Here, we determined that the structured domains of the Nup214 subcomplex reside in a protrusion of the cytoplasmic ring. At this site, they are ideally positioned at the cytoplasmic face of the central channel for anchoring their FG repeats onto the scaffold in order to conduct their function in nuclear transport. We furthermore predicted the positions of the anchoring domains of the FG-Nups 358 and POM121 at specific regions of the scaffold (Extended Experimental Procedures). Such positional information is a crucial prerequisite for computer simulations that have to take local properties of the central channel into account in order to model nucleocytoplasmic exchange accurately (Tagliazucchi et al., 2013).

In the future, similar integrated structural approaches as in this study can be systematically applied to other Nup subcomplexes in order to determine the positioning of FG-anchoring sites within the central channel and to analyze the architectural arrangement of the spoke ring complex. The information obtained by such methods needs to be complemented by high-resolution studies that specifically target intra- and intersubcomplex interfaces in order to ultimately obtain a pseudoatomic model of the entire human NPC.

EXPERIMENTAL PROCEDURES

Please see the Extended Experimental Procedures for details.

Cell Culture and Biochemical Isolations

The human Nup107 subcomplex was affinity-purified from nocodazole arrested Hek293 Flp Trex cells (Invitrogen) that were genetically engineered to express His6-HA-StrepII-Nup85 as described previously (Herzog et al., 2012). HeLa Flp-Trex cells (Zemp et al., 2009) were genetically engineered to express a synthetic micro-RNA targeting *nup214* for gene silencing using the BlockIT system (Invitrogen). Human nuclear envelopes were purified from HeLa cells as described previously (Ori et al., 2013).

Electron Microscopy

Samples for electron microscopy were prepared by negative staining with Uranyl acetate or cryo-plunge freezing. Electron microscopic data were acquired using a Titan Krios TEM (FEI), equipped with Gatan Camera 2k × 2k and GIF 2002 energy filter (Gatan) and further processed using the IMOD and TOM software packages.

Mass Spectrometry

Crosslinking reactions were carried out with isotope-coded disuccinimidylsubarate (Creative Molecules) as described previously (Walzthoeni et al., 2012). Crosslinked peptides were enriched by gel filtration and, in the case of nuclear envelope samples, separated using off-gel electrophoresis before gel filtration. Phosphopeptides were enriched using Titan dioxide chromatography. Mass spectrometric data were acquired using an Orbitrap Velos Pro (Thermo Scientific) and further processed using MaxQuant and xQuest/xProphet.

ACCESSION NUMBERS

Related to this manuscript are Electron Microscopy Data Bank entries EMD-2443, EMD-2444, and EMD-2445. The molecular fits of the vertex and high-resolution structures are available upon request.

SUPPLEMENTAL INFORMATION

Supplemental Information includes Extended Experimental Procedures, six figures, one data file, three tables, and three movies and can be found with this article online at http://dx.doi.org/10.1016/j.cell.2013.10.055.

ACKNOWLEDGMENTS

We thank Drs. Katja Beck and Edward A. Lemke for critical advice, reading of the manuscript, and numerous insightful discussions. We thank Drs. Carsten Sachse, Virginia VanDelinder, Thomas Cattabiani, and Iain Mattaj for critical reading of the manuscript; Ulrike Kutay for reagents; Peer Bork, Tommy E. White, Jan Kosinski, and John Briggs for critical advice. We gratefully acknowledge support from EMBL's mechanical workshop, electron microscopy and proteomics core facilities, and the centre for statistical data analysis and, in particular, want to thank James Riches, Drs. Jeroen Krijgsveld, and Bernd Klaus. K.H.B was supported by postdoctoral fellowships from the Swiss National Science Foundation, the European Molecular Biology Organization, and Marie Curie Actions. A.O. was supported by postdoctoral fellowships from the Alexander von Humboldt Foundation and Marie Curie Actions. A.L.D. was supported by the Robert Crooks Stanley Fellowship at Stevens

Institute of Technology. M.B. acknowledges funding by the European Research Council (309271-NPCAtlas).

Received: July 8, 2013
Revised: August 22, 2013
Accepted: October 2, 2013
Published: December 5, 2013

REFERENCES

Adams, R.L., and Wente, S.R. (2013). Uncovering nuclear pore complexity with innovation. Cell *152*, 1218–1221.

Akey, C.W. (1989). Interactions and structure of the nuclear pore complex revealed by cryo-electron microscopy. J. Cell Biol. *109*, 955–970.

Akey, C.W. (1995). Structural plasticity of the nuclear pore complex. J. Mol. Biol. *248*, 273–293.

Akey, C.W., and Radermacher, M. (1993). Architecture of the Xenopus nuclear pore complex revealed by three-dimensional cryo-electron microscopy. J. Cell Biol. *122*, 1–19.

Alber, F., Dokudovskaya, S., Veenhoff, L.M., Zhang, W., Kipper, J., Devos, D., Suprapto, A., Karni-Schmidt, O., Williams, R., Chait, B.T., et al. (2007). The molecular architecture of the nuclear pore complex. Nature *450*, 695–701.

Amlacher, S., Sarges, P., Flemming, D., van Noort, V., Kunze, R., Devos, D.P., Arumugam, M., Bork, P., and Hurt, E. (2011). Insight into structure and assembly of the nuclear pore complex by utilizing the genome of a eukaryotic thermophile. Cell *146*, 277–289.

Antonin, W., Ungricht, R., and Kutay, U. (2011). Traversing the NPC along the pore membrane: targeting of membrane proteins to the INM. Nucleus *2*, 87–91.

Beck, M., Förster, F., Ecke, M., Plitzko, J.M., Melchior, F., Gerisch, G., Baumeister, W., and Medalia, O. (2004). Nuclear pore complex structure and dynamics revealed by cryoelectron tomography. Science *306*, 1387–1390.

Beck, M., Lucić, V., Förster, F., Baumeister, W., and Medalia, O. (2007). Snapshots of nuclear pore complexes in action captured by cryo-electron tomography. Nature *449*, 611–615.

Bilokapic, S., and Schwartz, T.U. (2012). Molecular basis for Nup37 and ELY5/ELYS recruitment to the nuclear pore complex. Proc. Natl. Acad. Sci. USA *109*, 15241–15246.

Brohawn, S.G., Leksa, N.C., Spear, E.D., Rajashankar, K.R., and Schwartz, T.U. (2008). Structural evidence for common ancestry of the nuclear pore complex and vesicle coats. Science *322*, 1369–1373.

Debler, E.W., Ma, Y., Seo, H.S., Hsia, K.C., Noriega, T.R., Blobel, G., and Hoelz, A. (2008). A fence-like coat for the nuclear pore membrane. Mol. Cell *32*, 815–826.

Devos, D., Dokudovskaya, S., Alber, F., Williams, R., Chait, B.T., Sali, A., and Rout, M.P. (2004). Components of coated vesicles and nuclear pore complexes share a common molecular architecture. PLoS Biol. *2*, e380.

Dultz, E., and Ellenberg, J. (2010). Live imaging of single nuclear pores reveals unique assembly kinetics and mechanism in interphase. J. Cell Biol. *191*, 15–22.

Flemming, D., Thierbach, K., Stelter, P., Böttcher, B., and Hurt, E. (2010). Precise mapping of subunits in multiprotein complexes by a versatile electron microscopy label. Nat. Struct. Mol. Biol. *17*, 775–778.

Glavy, J.S., Krutchinsky, A.N., Cristea, I.M., Berke, I.C., Boehmer, T., Blobel, G., and Chait, B.T. (2007). Cell-cycle-dependent phosphorylation of the nuclear pore Nup107-160 subcomplex. Proc. Natl. Acad. Sci. USA *104*, 3811–3816.

Goldberg, M.W., and Allen, T.D. (1993). The nuclear pore complex: three-dimensional surface structure revealed by field emission, in-lens scanning electron microscopy, with underlying structure uncovered by proteolysis. J. Cell Sci. *106*, 261–274.

Güttinger, S., Laurell, E., and Kutay, U. (2009). Orchestrating nuclear envelope disassembly and reassembly during mitosis. Nat. Rev. Mol. Cell Biol. *10*, 178–191.

Herzog, F., Kahraman, A., Boehringer, D., Mak, R., Bracher, A., Walzthoeni, T., Leitner, A., Beck, M., Hartl, F.U., Ban, N., et al. (2012). Structural probing of a protein phosphatase 2A network by chemical cross-linking and mass spectrometry. Science *337*, 1348–1352.

Hinshaw, J.E., and Milligan, R.A. (2003). Nuclear pore complexes exceeding eightfold rotational symmetry. J. Struct. Biol. *141*, 259–268.

Hoelz, A., Debler, E.W., and Blobel, G. (2011). The structure of the nuclear pore complex. Annu. Rev. Biochem. *80*, 613–643.

Kampmann, M., and Blobel, G. (2009). Three-dimensional structure and flexibility of a membrane-coating module of the nuclear pore complex. Nat. Struct. Mol. Biol. *16*, 782–788.

Kampmann, M., Atkinson, C.E., Mattheyses, A.L., and Simon, S.M. (2011). Mapping the orientation of nuclear pore proteins in living cells with polarized fluorescence microscopy. Nat. Struct. Mol. Biol. *18*, 643–649.

Krull, S., Thyberg, J., Björkroth, B., Rackwitz, H.R., and Cordes, V.C. (2004). Nucleoporins as components of the nuclear pore complex core structure and Tpr as the architectural element of the nuclear basket. Mol. Biol. Cell *15*, 4261–4277.

Laurell, E., Beck, K., Krupina, K., Theerthagiri, G., Bodenmiller, B., Horvath, P., Aebersold, R., Antonin, W., and Kutay, U. (2011). Phosphorylation of Nup98 by multiple kinases is crucial for NPC disassembly during mitotic entry. Cell *144*, 539–550.

Loïodice, I., Alves, A., Rabut, G., Van Overbeek, M., Ellenberg, J., Sibarita, J.B., and Doye, V. (2004). The entire Nup107-160 complex, including three new members, is targeted as one entity to kinetochores in mitosis. Mol. Biol. Cell *15*, 3333–3344.

Löschberger, A., van de Linde, S., Dabauvalle, M.C., Rieger, B., Heilemann, M., Krohne, G., and Sauer, M. (2012). Super-resolution imaging visualizes the eightfold symmetry of gp210 proteins around the nuclear pore complex and resolves the central channel with nanometer resolution. J. Cell Sci. *125*, 570–575.

Maimon, T., Elad, N., Dahan, I., and Medalia, O. (2012). The human nuclear pore complex as revealed by cryo-electron tomography. Structure *20*, 998–1006.

Mansfeld, J., Güttinger, S., Hawryluk-Gara, L.A., Panté, N., Mall, M., Galy, V., Haselmann, U., Mühlhäusser, P., Wozniak, R.W., Mattaj, I.W., et al. (2006). The conserved transmembrane nucleoporin NDC1 is required for nuclear pore complex assembly in vertebrate cells. Mol. Cell *22*, 93–103.

Miller, B.R., Powers, M., Park, M., Fischer, W., and Forbes, D.J. (2000). Identification of a new vertebrate nucleoporin, Nup188, with the use of a novel organelle trap assay. Mol. Biol. Cell *11*, 3381–3396.

Mitchell, J.M., Mansfeld, J., Capitanio, J., Kutay, U., and Wozniak, R.W. (2010). Pom121 links two essential subcomplexes of the nuclear pore complex core to the membrane. J. Cell Biol. *191*, 505–521.

Nagy, V., Hsia, K.C., Debler, E.W., Kampmann, M., Davenport, A.M., Blobel, G., and Hoelz, A. (2009). Structure of a trimeric nucleoporin complex reveals alternate oligomerization states. Proc. Natl. Acad. Sci. USA *106*, 17693–17698.

Olsen, J.V., Vermeulen, M., Santamaria, A., Kumar, C., Miller, M.L., Jensen, L.J., Gnad, F., Cox, J., Jensen, T.S., Nigg, E.A., et al. (2010). Quantitative phosphoproteomics reveals widespread full phosphorylation site occupancy during mitosis. Sci. Signal. *3*, ra3.

Ori, A., Banterle, N., Iskar, M., Andrés-Pons, A., Escher, C., Khanh Bui, H., Sparks, L., Solis-Mezarino, V., Rinner, O., Bork, P., et al. (2013). Cell type-specific nuclear pores: a case in point for context-dependent stoichiometry of molecular machines. Mol. Syst. Biol. *9*, 648.

Panté, N., and Kann, M. (2002). Nuclear pore complex is able to transport macromolecules with diameters of about 39 nm. Mol. Biol. Cell *13*, 425–434.

Paulillo, S.M., Phillips, E.M., Köser, J., Sauder, U., Ullman, K.S., Powers, M.A., and Fahrenkrog, B. (2005). Nucleoporin domain topology is linked to the transport status of the nuclear pore complex. J. Mol. Biol. *351*, 784–798.

Rasala, B.A., Orjalo, A.V., Shen, Z.X., Briggs, S., and Forbes, D.J. (2006). ELYS is a dual nucleoporin/kinetochore protein required for nuclear pore assembly and proper cell division. Proc. Natl. Acad. Sci. USA *103*, 17801–17806.

Reichelt, R., Holzenburg, A., Buhle, E.L., Jr., Jarnik, M., Engel, A., and Aebi, U. (1990). Correlation between structure and mass distribution of the nuclear pore complex and of distinct pore complex components. J. Cell Biol. *110*, 883–894.

Rout, M.P., Aitchison, J.D., Suprapto, A., Hjertaas, K., Zhao, Y., and Chait, B.T. (2000). The yeast nuclear pore complex: composition, architecture, and transport mechanism. J. Cell Biol. *148*, 635–651.

Sachdev, R., Sieverding, C., Flötenmeyer, M., and Antonin, W. (2012). The C-terminal domain of Nup93 is essential for assembly of the structural backbone of nuclear pore complexes. Mol. Biol. Cell *23*, 740–749.

Schwartz, T.U. (2005). Modularity within the architecture of the nuclear pore complex. Curr. Opin. Struct. Biol. *15*, 221–226.

Schwarz-Herion, K., Maco, B., Sauder, U., and Fahrenkrog, B. (2007). Domain topology of the p62 complex within the 3-D architecture of the nuclear pore complex. J. Mol. Biol. *370*, 796–806.

Senger, S., Csokmay, J., Akbar, T., Jones, T.I., Sengupta, P., and Lilly, M.A. (2011). The nucleoporin Seh1 forms a complex with Mio and serves an essential tissue-specific function in Drosophila oogenesis. Development *138*, 2133–2142.

Seo, H.S., Ma, Y., Debler, E.W., Wacker, D., Kutik, S., Blobel, G., and Hoelz, A. (2009). Structural and functional analysis of Nup120 suggests ring formation of the Nup84 complex. Proc. Natl. Acad. Sci. USA *106*, 14281–14286.

Solmaz, S.R., Chauhan, R., Blobel, G., and Melčák, I. (2011). Molecular architecture of the transport channel of the nuclear pore complex. Cell *147*, 590–602.

Stagg, S.M., Gürkan, C., Fowler, D.M., LaPointe, P., Foss, T.R., Potter, C.S., Carragher, B., and Balch, W.E. (2006). Structure of the Sec13/31 COPII coat cage. Nature *439*, 234–238.

Szymborska, A., de Marco, A., Daigle, N., Cordes, V.C., Briggs, J.A., and Ellenberg, J. (2013). Nuclear pore scaffold structure analyzed by super-resolution microscopy and particle averaging. Science *341*, 655–658.

Tagliazucchi, M., Peleg, O., Kröger, M., Rabin, Y., and Szleifer, I. (2013). Effect of charge, hydrophobicity, and sequence of nucleoporins on the translocation of model particles through the nuclear pore complex. Proc. Natl. Acad. Sci. USA *110*, 3363–3368.

Talamas, J.A., and Hetzer, M.W. (2011). POM121 and Sun1 play a role in early steps of interphase NPC assembly. J. Cell Biol. *194*, 27–37.

Thierbach, K., von Appen, A., Thoms, M., Beck, M., Flemming, D., and Hurt, E. (2013). Protein interfaces of the conserved Nup84 complex from Chaetomium thermophilum shown by crosslinking mass spectrometry and electron microscopy. Structure *21*, 1672–1682.

Unwin, P.N., and Milligan, R.A. (1982). A large particle associated with the perimeter of the nuclear pore complex. J. Cell Biol. *93*, 63–75.

Walzthoeni, T., Claassen, M., Leitner, A., Herzog, F., Bohn, S., Förster, F., Beck, M., and Aebersold, R. (2012). False discovery rate estimation for cross-linked peptides identified by mass spectrometry. Nat. Methods *9*, 901–903.

Zemp, I., Wild, T., O'Donohue, M.F., Wandrey, F., Widmann, B., Gleizes, P.E., and Kutay, U. (2009). Distinct cytoplasmic maturation steps of 40S ribosomal subunit precursors require hRio2. J. Cell Biol. *185*, 1167–1180.